

Evolution of the Oceanic Lithosphere in the equatorial Atlantic, evidence for small-scale convection from the PI-LAB experiment

Nicholas Harmon, Catherine Rychert, J. Michael Kendall, Matthew Agius, Petros Bogiatzis
Saikiran Tharimena

Key Points

- We image a lithosphere that increases from 30 to 50 km thick beneath from 0-40 My age seafloor
- We image punctuated low velocity zones beneath the ridge and up to 400 km off-axis in the asthenosphere that likely require melt
- The pattern of anomalies suggests small-scale convection may occur beneath a range of seafloor ages

Abstract

The oceanic lithosphere is a primary component of the plate tectonic system, yet its evolution and its asthenospheric interaction has rarely been quantified by in-situ imaging at slow spreading systems. We use Rayleigh wave tomography from noise and teleseismic surface waves to image the shear wave velocity structure of the oceanic lithosphere-asthenosphere system from 0 to 80 My at the Equatorial Mid-Atlantic Ridge using data from the Passive Imaging of the Lithosphere-Asthenosphere Boundary (PI-LAB) experiment. We observe fast lithosphere ($V_{SV} > 4.4$ km/s) that thickens from ~ 30 km near the ridge axis to $> 50 - 80$ km at seafloor > 60 My. We observe several punctuated low velocity anomalies ($V_{SV} < 4.1$ km/s) in the asthenosphere between 50-150 km depth, not necessarily focused beneath the ridge axis. Some of the low velocity regions are located within 100 km of the ridge axis, but other low velocity regions are observed at distances > 400 km from the ridge. We observe a high velocity lithospheric downwelling drip beneath 30 My seafloor that extends to 80-130 km depth. The asthenospheric low velocities likely require partial melt. Although melt is present off axis, the lack of off-axis volcanism suggests the lithosphere acts as a permeability boundary for deeper melts. The punctuated and off-axis character of the asthenospheric anomalies and lithospheric drip suggest small-scale convection is active at a range of seafloor ages. Small-scale convection and/or more complex mantle flow may be aided by the presence of large offset fracture zones and/or melt buoyancy.

Plain Language Summary

Tectonic plates are created at mid ocean ridges. As the plates age and move over the weaker asthenosphere below they thicken and subside. Yet, there are few high-resolution images of this process. We deployed 39 ocean bottom seismometers in the equatorial mid Atlantic to image the seismic velocity of the tectonic plate and the asthenosphere below.

We observe a tectonic plate that generally thickens with age, but the thickening is not simple and monotonic everywhere, and there may be evidence of drips coming off the base of the plate. We also see evidence for small pockets of melt and rising mantle far away from the ridge axis. Taken together this suggests that flow in the mantle is more complicated than previously thought. Small-scale convection may occur beneath a range of seafloor ages, which may also affect the way the lithosphere cools and ages. Thus, our result has implications for how tectonic plates evolve and interact with the mantle below and how plate tectonics works to cool the earth since its formation billions of years ago.

1. Introduction

The origin and evolution of the oceanic lithosphere is fundamental to our understanding of plate tectonics. First and foremost, oceanic lithosphere makes up most of the Earth's lithosphere. In addition, the ocean plates play a large role in driving plate tectonics, for instance by sinking back into the earth at subduction zones and/or pushed to the side by upwelling mantle beneath ridges (Forsyth & Uyeda, 1975). The chemical alteration of the oceanic lithosphere to serpentine also provides volatiles that result in seismicity, mantle melting, and arc volcanism when the plates subduct back into the Earth (Stern, 2002). The relative density contrast between oceanic lithosphere and continental lithosphere also determines the depth of the oceans through geologic time via isostasy (Karlsen et al., 2019).

To first order, young oceanic lithosphere may be described by simple thermal models, such as the half-space cooling model (Turcotte & Oxburgh, 1967) which predicts that the lithosphere should cool, subside and thicken with age. Several observations, such as subsidence of the seafloor and heatflow measurements are generally consistent with thermal models at least beneath young seafloor, <70 My (Parsons & Sclater, 1977; Stein & Stein, 1992).

However, greater complexities have also been suggested even beneath young seafloor. More advanced 2-D geodynamic models show the thermal evolution of the young oceanic lithosphere varies depending on the spreading rate. At slower spreading rates, lateral conductive cooling is thought to play an important role in creating thicker lithosphere directly beneath the ridge axis (Parmentier & Morgan, 1990), which may also explain the formation of flexurally compensated median valley structures observed at the Mid Atlantic Ridge (Morgan et al., 1987). At faster spreading rates, the lithosphere may be thinner or non-existent beneath the ridge as was suggested at the superfast spreading East Pacific Rise (EPR) (Forsyth, 1992; Forsyth et al., 1998) and the ridge morphology is dominated by linear axial volcanic structures (Forsyth, 1992). In addition, the spreading rate may dictate the nature of mantle upwelling beneath the ridge, with faster spreading oceanic plates producing more 2-D sheet like upwelling, often called "passive" upwelling, while slow spreading may generate more 3-D diapiric upwelling referred to as "active" upwelling (Parmentier & Morgan, 1990). Mantle melting may also affect the dynamics of the system, via melt and/or depletion enhanced buoyancy, which may focus upwelling for "active" upwelling (Buck & Su, 1989; Jha et al., 1994; Parmentier & Morgan, 1990). In addition melting may also reduce the viscosity of the lithosphere by creating a chemically distinct lithosphere that extends to a relatively constant depth, down to which melt has been extracted (Gaherty et al., 1996). Many of these processes could be occurring simultaneously, defining the lithosphere at younger ages.

There is similar complexity beneath older seafloor, where the simple half-space cooling model breaks down, and seafloor and heatflow flattening occurs (Parsons & Sclater, 1977; Stein & Stein, 1992). Modified versions of the half-space cooling model such as the plate cooling model and the Chablis cooling model (Doin & Fleitout, 1996; Hasterok et al., 2011; Parsons & Sclater, 1977; Stein & Stein, 1992), match the seafloor subsidence and heatflow data at older ages. The plate model empirically fits the heat flow and seafloor subsidence data via an exponential series expansion, while the Chablis model, which is more physically based imposes a heat flux boundary condition (Doin & Fleitout, 1996; Hasterok et al., 2011; Parsons & Sclater, 1977; Stein & Stein, 1992). However, the underlying physical mechanism that produces this seafloor flattening has long been a subject of debate. Several possible mechanisms have been proposed, for instance small-scale convection (Richter, 1973), as well as resurfacing of the seafloor and thermal erosion by intraplate volcanism (Korenaga & Korenaga, 2008).

Small-scale convection is most commonly invoked to explain seafloor flattening (e.g., Ritzwoller et al., 2004). The presence of small-scale convection could impact the evolution of the oceanic lithosphere as it limits the thickness of the thermal boundary layer (Richter, 1973). Small-scale convection is thought to occur due to the formation of gravitational instabilities from a cooling oceanic lithosphere that downwell into the mantle, as the lithosphere reaches a critical thickness (Richter, 1973). The onset age of the instabilities and the length scale of the convection cells are dependent on the viscosity structure (Ballmer et al., 2009; Doin & Fleitout, 1996; King & Anderson, 1998; Korenaga & Jordan, 2003; Ritzwoller et al., 2004; van Hunen et al., 2003). Geodynamic models predict ages/critical thicknesses of onset of convection range from as young as 5 My to 60 My and older (Buck & Parmentier, 1986; Davaille & Jaupart, 1994). The predicted scale of the convection cells is typically on the order of < 500 km, below the resolution of most global seismic tomography models. With fast spreading, the convective cells may be organized into a helical pattern of flow in the direction of the plate motion (Richter, 1973), referred to as “Richter Rolls”. The presence of small-scale convection beneath the oceanic lithosphere has many implications for the heat budget through time and viscosity structure and is therefore key to our understanding of the underlying drivers of plate tectonics and mantle convection.

Much of our understanding of the origin and evolution of oceanic lithosphere at high-resolution comes from a handful of experiments in the Pacific. The MELT experiment at 17° S on the ultrafast spreading southern East Pacific Rise (EPR) (Forsyth et al., 1998) and the subsequent GLIMPSE experiment imaged oceanic lithosphere from 0-10 My (Weeraratne et al., 2007). More recently, the Cascadia Initiative imaged the intermediate spreading Juan De Fuca Ridge with oceanic lithosphere from 0-10 My (Toomey et al., 2014). However, slow spreading ridges, particularly, the non-hotspot affected parts of the Mid Atlantic Ridge have not been imaged at a similar scope and scale up until this point.

In this paper we present results of Rayleigh wave imaging of the crust and upper mantle of the equatorial Mid Atlantic using data collected as part of the Passive Imaging of the Lithosphere-Asthenosphere Boundary Experiment (PI-LAB) and the Experiment to Unearth the Rheological Oceanic Lithosphere-Asthenosphere Boundary (EURO-LAB) (Fig. 1). The experiments consisted of 39 broadband ocean bottom seismometers and 39 co-located ocean bottom magnetotelluric instruments deployed from March 2016 to March 2017 (Agius et al., 2018; Harmon et al., 2018). The array is located around the Romanche and Chain Fracture zones, extending across the Mid Atlantic ridge. Using our shear velocity model, we examine the thickness of the seismically fast lithosphere from 0-80 My seafloor

and the structure of the underlying asthenosphere across the region to examine the origin and evolution of the lithosphere and the mantle dynamics beneath. We show that the system is more dynamic than classic models of the ocean lithosphere that typically assume evolution according to the 1-D half-space cooling model, and we examine the role small-scale convection in our study region.

2. Methods and Resolution

Vertical component data from the ocean bottom seismometers are used to measure dispersion of Rayleigh waves for both ambient noise and teleseismic imaging. Example data are shown in Fig. 2 for both a teleseismic event and ambient noise. We pre-process the vertical components for ambient noise correlation in the following way: for each day-long continuous vertical seismogram we decimate to 1 Hz sampling rate, remove the instrument response and bandpass filter the data between 0.01 – 0.33 Hz. We follow Bensen et al. (2007) by normalizing the amplitude with the running mean of the envelope of the data. The data are then whitened and tapered prior to cross correlating all possible station combinations. Each day's cross correlations are stacked to generate the noise correlation functions (NCF). We use the symmetric part of the NCF for further analysis to reduce the effects of inhomogeneous noise sources (Harmon et al., 2010). For the teleseismic data, 3 hours of data are extracted from all teleseismic events that occurred during the PI-LAB deployment from epicentral distances between 30 – 150°. Again, the data are detrended and demeaned before the instrument responses are removed.

We use frequency-time analysis on the Rayleigh waves from both teleseismic and NCF to measure dispersion (Landisman et al., 1969; Levshin & Ritzwoller, 2001). We correct the NCF dispersion measurements for apparent phase shifts caused by cross correlation (Harmon et al., 2008; Harmon et al., 2010). We measure amplitude and phase of the teleseismic data, while only phase was measured from the NCF. In total, there are 279 usable NCF and up to 205 unique earthquake events resulting in up to 1719 teleseismic observations at a given period. Raypath coverage is shown in Fig. 3. We measure dispersion from 10 – 33 s period for the NCF and from 18 – 143 s period for the teleseismic data. We use the apparent wavelength of the teleseismic and NCF dispersion measurements to estimate an average phase velocity curve across the region (Harmon et al., 2008; Harmon et al., 2010).

The inversion for shear velocity is a two-step process. First, we invert for phase velocity maps across the period range of interest. Then we invert for shear velocity as a function of depth at each point using the dispersion at all periods across the phase velocity maps. The collected 1-D shear velocity inversions form a 3-D volume. The Rayleigh wave amplitude and phase dispersion measurements from 18 – 143 s period are inverted using the two plane wave method (Forsyth & Li, 2005) with 2-D finite frequency sensitivity kernels (Yang & Forsyth, 2006; Zhou et al., 2004). At periods < 40 s, we incorporate the NCF phase data into the inversion (Harmon & Rychert, 2016) using finite frequency sensitivity kernels and the same nodal parameterization.

We use the best fitting 1-D shear velocity from our 1-D dispersion curve for the entire region from 18-143 s period as the starting model for our 3-D shear velocity inversion. We use an iterative damped least squares inversion for both our 1-D starting model inversion and our 3-D inversion at each pixel in the map (Tarantola & Valette, 1982). We use DISPER80 (Saito, 1988) to calculate Fréchet derivatives for the inversion. Our starting shear velocity models consist of a water layer, taken from the average water depth of each grid

point, and a two-layer crust of 6 km total thickness, with the best fit 1-D shear velocity model below. We assume a fixed V_P/V_S ratio of 1.8. Testing indicates that a different V_P/V_S assumption (± 0.1) results in minimal changes in the shear velocity, well within error.

We present two different parameterizations for the mantle shear velocity inversion to explore the effects of choice of parameterization on the final models. Our two parameterizations are: 1) a smooth, spline parameterization and 2) a rougher, unsmoothed discontinuous layered model. These two different approaches are used in both local and global surface wave inversions. We wanted to explore the range of results from these very different parameter choices that still fit the data within error. The smooth model assumption is generally aligned with the notion that conductive cooling is dominant factor in lithospheric structure and structure (i.e., the predicted thermal gradients are smooth), whereas a discontinuous structure allows for sharp gradients at the base of the lithosphere that have been observed in other oceanic lithospheric settings from receiver functions (e.g., Rychert et al., 2018). For the discontinuous parameterization we have 10 km thick layers in the upper 100 km of the mantle, transitioning to 50 km thick layers in deeper layers. For the spline parameterization, we allow for 12 knots over 400 km of the mantle. The knot spacing is adjusted as the model updates to improve the spline approximation.

We examine the resolution of the tomography for phase velocity with checkerboard recovery tests and synthetic structure recovery tests. We use anomalies of 1° and 2° length scales with amplitudes of ± 0.1 km/s from the average velocity at each period (Fig. 4). In our structure recovery test, an age dependent phase velocity structure is used. The phase velocity increases non-linearly, as a square root of age, from 3.7 to 4.15 km/s from 0 – 90 My, covering the range of age in our study region. The range in phase velocity is similar to the change in our observed phase velocity maps. We show these tests for phase velocity maps at 20 and 40 s period in Fig. 5. We smooth the structure with a 2-D gaussian filter. In both recovery tests, random noise is added to the synthetic data, at a level that produces residual errors similar in magnitude to those observed in the inversion of the real data.

We observe good recovery of the pattern of 1° anomalies from 20 – 57 s period, with little smearing evident (Fig. 4). The magnitude of the recovered anomalies in the best resolved regions are within 5%, but outside the array they are recovered to within 50%. Smearing is minimal within the array but is visible in a north-south direction at all periods, and strongest in the southern part of the study region outside the array. At longer periods, (>91 s), 2° anomalies are well recovered (Fig. 4). Magnitudes of the anomalies are recovered at > 91 s within 10 – 50 % within the array. There is little smearing evident inside the array, but outside of the array, particularly to the south, north-south smearing is visible at periods > 91 s. Features of ~ 100 km scale are interpretable in the upper 150 km, where the 20 – 91 s period data have their greatest sensitivity.

Our age dependent phase velocity recovery test indicates variations in the phase velocity structure due to ridge structure and fracture zone offsets are well recovered in our models (Fig. 5). We recover the magnitude of the anomalies to within 10% within the array. Low velocity regions offset by the Chain Transform (~ 3.7 km/s) are resolved with each ridge segment having a distinct low velocity zone. The reduction in phase velocity going south across the Romanche Fracture Zone is recovered both 20 and 40 s period. Within the array there is little evidence of smearing of the ridge anomalies across the fracture zones between the segments. We observe smearing near the southern ridge segment, and the anomaly recovered for the ridge is less continuous. Features > 100 km in length scale in the upper 150 km of the shear velocity model are well-resolved.

3. Results

3.1 Phase Velocity

Our average phase velocities range from 3.97 ± 0.01 km/s at 18 s period to 4.33 ± 0.01 km/s at 143 s period (Fig. 6). We observe a decrease in phase velocity at 25 – 57 s period, as typically observed in oceanic dispersion curves, suggestive of a low velocity zone in the upper mantle.

At 20-40 s period the phase velocity maps exhibit slow velocities near the ridge axis with increasing velocities further away (Fig. 7). We observe the slowest velocities (3.71 ± 0.07 km/s) on the ridge segment south of Chain at 20 s period. At 40 s period, slow velocities are observed near the ridge, north and south of Chain, but not necessarily focused directly beneath the ridge and in a broader ~ 200 km wide zone offset to the west of the ridge. Velocities are higher north of the Romanche Fracture Zone, and at both 20 and 40 s period we observe a high velocity region off axis at 10° W Longitude, 0° Latitude.

At the longer periods (57 and 100 s) there are several discrete low velocity regions not necessarily associated with the ridge axis. Low velocities (<4.0 km/s) persist in the general vicinity of the ridge segments visible in the 57 s and 100 s period maps. We also observe a distinct off-axis low velocity zone 200 km away from the ridge axis at near 10° W Longitude, 2° S Latitude, (Fig. 7). Across the Romanche Fracture Zone, the velocities remain higher to ~ 100 s period. Finally, the high velocity region (4.10 - 4.20 ± 0.07 km/s) at 10° W Longitude, 0° Latitude persists in the 57 s and 100 s period maps.

3.2 Shear Velocities

The preferred 1-D shear velocity model exhibits a fast lithosphere with maximum velocities of 4.64 ± 0.12 km/s in the upper 50 km of the mantle with a low velocity zone from 50 – 140 km depth with minimum velocities of 4.23 ± 0.12 km/s.

The 3-D shear velocity models from the discontinuous parameterizations (Fig. 8) and the spline parameterizations (Fig. 9) show features that are classic of oceanic lithosphere. Specifically, both parameterizations show a fast lithosphere underlain by a low velocity zone, typically associated with the asthenosphere. In general, the fast lithosphere increases in thickness away from the ridge axis. We present models from both parameterisations and compare and contrast them to demonstrate the possible range of structures that could explain the data.

The fast lithosphere structure ($V_s > 4.4$ km/s) is visible in the upper 20-80 km of our shear velocity model. We show the shear velocities as depth slices at 26 and 76 km depth and three profiles in Figs. 9 and 10, labelled I, II and III, which show cross sections across the ridge (I and II) and parallel to the ridge (III). In the 26 km depth slice (Fig 8A and 9A) velocities range from 4.4 – 4.8 km/s, with lower average velocities near the ridge axis. In general, the thickness and velocity of the fast lithosphere increase away from the Mid Atlantic Ridge. If we choose the 4.4 km/s velocity contour visible in the profiles (Fig 8C-E and Fig 9C-E) as the measure of the lithosphere thickness, the lithosphere beneath the Mid Atlantic Ridge is 20-30 km thick as shown in Profile I and II for both parameterizations. In both Profile I and II the fast lid thickness increases to ~ 40 -50 km up until 10 My seafloor and thins slightly by 10 km at 10-20 My. In Profile I, at 30 My, the lithosphere thickness increases to 80 km in the spline parameterization and 130 km in the discontinuous parameterization. In Profile III, the lithosphere thickness increases going northward from 30 km at 0 My seafloor to ~ 50 km at 15 My seafloor crossing the Chain Fracture Zone to ~ 70 km on 61 My seafloor going across the Romanche Fracture Zone.

In the low velocity zone at 50-150 km depth velocities range from 4.08 – 4.40 km/s, with low velocity regions beneath the ridge axis and a few punctuated low velocity regions off-axis with minimum velocities of $4.08\text{--}4.12 \pm 0.05$ km/s. These are visible in the 76 km depth slice (Fig. 8B and 9B). The low velocity beneath the ridge in Profile I (labelled a in Fig. 8 and 9) is slower by ~ 0.10 km/s than the subridge anomaly (labelled b) in Profile II south of the Chain Fracture Zone. In the spline parameterization the low velocity region beneath the ridge is deeper, centered at ~ 110 km, while in the discontinuous parameterization the low velocities are centred at ~ 70 km. The low velocity anomalies beneath the ridge are not symmetric. In the discontinuous parameterisation in profile I the low velocity anomaly beneath the ridge is skewed towards the west and 200 km in lateral extent with a smaller anomaly ~ 100 km to the east of the ridge. In the spline parameterization in profile I the low velocity region beneath the ridge is asymmetric towards the east with a smaller anomaly towards the west. The low velocity zones beneath the ridge in Profile II are located ~ 100 km away to the east and west from the ridge in both the discontinuous and spline models. There are two off-axis low velocity regions; one in Profile I at 12.5° W Longitude (labelled c) and Profile II 10° W Longitude (labelled d), up to 400 km away from the axis. These regions are approximately 100-200 km in lateral extent and about 50-100 km in depth in the discontinuous parameterization and 100-150 km depth in the spline parameterization. There is also a high velocity region visible in Profile II at 10.5° W Longitude that extends from 50 -150 km depth in both parameterizations, with a width of ~ 100 km (labelled LD).

There are several key differences between the two shear wave model parameterizations. The spline parameterization model is much smoother than the discontinuous parameterization (Fig. 8 vs Fig. 9). The fast lid has a much sharper base in the discontinuous model, in some cases decreasing $>10\%$ over 20 km where the lid transitions into one of the lowest velocity zones. In the spline parameterization model, the same velocity drop occurs over 30-40 km. The difference in fast lid thickness also affects the depths in the low velocity zone anomalies. For example, the low velocity regions are centered at 110 km depth in the spline parameterization, while in the discontinuous model the lowest velocity anomalies in Profile II are centered 70 km depth. Some of the difference between the two models is due to the 1-D sensitivity kernels for the shear velocity inversion which have a broad sensitivity with depth that is similar between the two model parameterizations (Fig. 6C) which allows trade-off between the thickness of the lid and the velocity. In other words, a thickening lid in the spline parameterisation fit the data as well as a higher velocity, thinner lid, which is seen in the discontinuous model (Fig 9). Specifically, in the discontinuous model velocities are high, >4.7 in the upper 30-40 km, while in the spline parameterization velocities are only > 4.7 in the upper 20-30 km. Although the differences show the full range of acceptable models, we prefer the discontinuous parameterisation owing to the constraints from receiver functions and magnetotelluric studies from the same experiment, which suggest a sharp drop in velocity is required (Rychert et al., 2019; Wang et al., 2020). Therefore, we proceed primarily discussing the discontinuous parameterisation model.

4. Discussion

4.1 Lithospheric Structure

We compare our result to the simple 1-D conductive half-space cooling model, the plate model (Parsons & Sclater, 1977; Stein & Stein, 1992) assuming a 90 km thick plate based on heat flow (Hasterok et al., 2011), and a 2-D numerical geodynamic model, which is

calculated for 0-40 My seafloor. For the 2-D case we calculate the thermal structure in the geodynamic model assuming a half-spreading rate of 20 mm/yr using the method of Jha et al. (1994) with a mantle potential temperature of 1350 °C. The geodynamic model incorporates lateral conductive cooling (Fig. 10). We convert the thermal models to shear velocity using the relationships of Jackson and Faul (2010) incorporating attenuation effects. We use the depth to the 4.4 km/s contour as a proxy for the base of the lithosphere because it roughly coincides with the 1200 °C isotherm, which also coincides with the predicted depth where a strong velocity and viscosity decrease occurs (e.g., Behn et al., 2009; Jackson & Faul, 2010).

Beneath the ridge axis, the observed 20 - 30 km fast lid is thicker than the non-existent lid predicted by the half-space cooling model. However, it is consistent with predictions of a non-zero sub-ridge lid thickness from geodynamic models of slow spreading that allow for lateral conductive cooling (Parmentier & Morgan, 1990). For instance, our geodynamic model predicts a lithospheric thickness near the ridge of 20 km below the sea surface using the 4.4 km/s velocity contour, which is within 10 km of our shear velocity models.

Beneath older seafloor ages (up to ~60 My) the fast lithosphere in our velocity model generally increases in velocity and thickness with increasing age but does not agree everywhere with predictions from the conductive cooling models (Fig 8, 9 anomalies labelled a-d, LD vs Fig 10). Half-space cooling, the geodynamic model, and the plate model predict that the lithosphere, should range from 0 -40 km thickness from 0-10 My, and then from 50-80 km from 10-40 My age (Fig. 10). Profile I and Profile II show the fast lid thickening from 20 to 40 km monotonically from 0 My to ~10 My. However, the fast lid in our velocity models then begins to thin from 10-20 My based on the depth to 4.4 km/s. In some places the fast lid is much thicker than predicted, for example in Profile I, the lithosphere appears to thicken by 20-100 km based again on the 4.4 km/s contour from 30-40 My, depending on which model parameterization is used (LD in Fig, 8 and 9). We interpret this thickening as a lithospheric downwelling, caused by a gravitational instability and small-scale convection (e.g., Richter, 1973).

Our observed lithosphere on seafloor > 60 My is thinner than predicted by the plate and half-space cooling models. For instance, the plate model would predict a 90 km thick plate, while the half-space cooling model predicts the lithosphere should increase from 80-113 km from 40 to 80 My. The depth to the 4.4 km/s contour in Profile III is at ~70 km at 61 My aged seafloor north of Romanche (Fig. 8 and 9), approximately 20 km thinner than the plate model predictions.

The thickness of our young lithosphere is equal to or greater than that observed at faster spreading centers. At the fast spreading EPR in the MELT region, using the same Rayleigh wave tomography method used here, the fast lid was nearly zero thickness beneath the crust, as compared to the 20 – 30 km thickness we observe here (Harmon et al., 2009). Beneath 10 My old lithosphere in our region (40 km) the thickness is similar to that found at the oldest ages interrogated at the EPR (40 – 50 km) (Harmon et al., 2009). Our result beneath the ridge axis is also ~10 km thicker than that found at the intermediate spreading Juan de Fuca Ridge from the same Rayleigh wave tomography method used here (Bell et al., 2016). The thickness of the lithosphere in our study region (20 - 30 near the ridge and 40 km beneath 10 My old seafloor) is in general agreement, possibly thicker beneath the ridge, in comparison to receiver function estimates of the depth of the lithosphere-asthenosphere boundary near the Juan de Fuca Ridge which found an increase

from 20 to 45 ± 5 km depth beneath 0 – 10 My seafloor (Rychert et al., 2018). In general, along with previous results from faster spreading centers, our result suggests that the lithosphere thickness beneath ridges increases as the spreading rate decreases, which is generally consistent with the notion that lateral conductive cooling becomes more important at lower spreading rates.

4.2 Asthenospheric Structure

The slow velocities in the asthenosphere near the ridge axis are generally consistent with the half-space cooling and geodynamic models that also predict the slowest velocities beneath the ridge, slightly increasing with age at a given depth (Fig. 10). However, the velocities in our velocity model are slower and more focused in lateral extent beneath the ridge than in the geodynamic model predictions (Fig. 10), which predict 200-300 km wide low velocity zones. The focused shape of the anomalies is more consistent with active upwelling aided by either melt or depletion buoyancy (Forsyth, 1992), which tends to produce a narrower and faster upwelling region beneath the ridge, on the order of 50-100 km lateral scale (Jha et al., 1994). The fact that the northern ridge segment is slower than the southern ridge segment (4.08 km/s vs. 4.17 km/s) may reflect lateral variation in the vigor of upwelling, which could also vary temporally, given that is not a steady state process. The anomalies are also asymmetric beneath the ridges suggesting greater complexity in mantle flow.

The punctuated off axis low velocity anomalies in the asthenosphere are not consistent with our geodynamic model of passive corner flow or half-space cooling (Fig. 10). Lateral variations in shear velocities off axis, suggest lateral variations in thermal structure, which could be related to small-scale convection (Barnouin-Jha & Parmentier, 1997; Buck & Parmentier, 1986). The velocity variations occur on length scales of 200-400 km, but the variations are not necessarily consistent with fully developed small-scale convection or “Richter Rolls.” In Richter Roll convection models, elongated upwelling and downwelling zones develop in the spreading direction that would be associated with elongated slower and faster velocities, respectively (Barnouin-Jha & Parmentier, 1997). Whereas, our observations are more consistent with punctuated features in the spreading direction. One possible explanation is that in slower spreading systems instabilities form as a random process and are not organized by the plate motion (Korenaga & Jordan, 2003).

To explain the lowest velocities in the asthenosphere in the region, likely requires more than just temperature. Assuming a pyrolite composition and the relationship of Stixrude and Lithgow-Bertelloni (Stixrude & Lithgow-Bertelloni, 2005) at 75 km depth and 1350 -1450 °C, the shear velocity should be 4.30-4.35 km/s. Accounting for attenuation effects, the shear velocities might be reduced to ~4.15 km/s assuming a grain size of 5 mm (Jackson & Faul, 2010) (Fig. 10). We observe velocities down to 4.08 ± 0.05 km/s at 75 km/s significantly below the melt free estimates in this temperature and depth range. Geochemical estimates of mantle temperatures beneath the ridge segments in our study region and nearby indicate temperature is relatively cold, slightly less than the 1350 °C potential temperature used here, but the mantle is relatively enriched, which would promote partial melting that would further reduce the shear velocity (Schilling et al., 1994; Schilling et al., 1995). We estimate up to ~0.25% partial in the mantle is needed to explain our lowest velocities both on and off the ridge axis (Hammond & Humphreys, 2000). The presence of melt at punctuated intervals may enhance buoyancy and aid in small-scale convection in the region.

The asymmetry of our asthenospheric anomalies with respect to the ridge and the presence of off axis low velocity anomalies bears some resemblance to previous surface wave imaging at the ultrafast spreading East Pacific Rise at 17 °S and the Juan de Fuca Ridge. The asthenospheric low velocity anomaly is strongest beneath the EPR, but there is distinct asymmetry observed between the Pacific and Nazca plate, with the larger part of the anomaly beneath the Pacific Plate. Asymmetry in asthenospheric anomalies have also been observed at the Juan de Fuca Ridge, near the Axial seamount, which has been attributed to interaction between the Cobb hotspot and the ridge (Bell et al., 2016; Hawley et al., 2016). Further off-axis, low velocities were observed beneath the slab in both Rayleigh and body wave tomography (Bell et al., 2016; Hawley et al., 2016) which were attributed to melt migration beneath the downgoing slab (Hawley et al., 2016). All three ridge systems, at the full range of spreading rates, have asymmetry in the asthenospheric sub-ridge anomaly and evidence for more complicated mantle flow and/partial melt off axis than simple corner flow models predict and likely involve some form of small-scale convection.

Melt may also pond at the base of the lithosphere in channels, as suggested from active source studies in the Pacific (Stern et al., 2015) and near our study region further to the north (Mehouachi & Singh, 2018). Low resistivity channels, consistent with the presence of partial melt have also been imaged within our study region using MT (Wang et al., 2020). The channels are likely fed by the buoyant upwellings we observe at greater depths. The amount of melt available may dictate whether volcanism is observed at the surface and the stability of channels through time (Havlin et al., 2013). The lack of off-axis volcanism above our low velocity anomalies in our study area is much different than those observed at the EPR (Harmon et al., 2018), but similar to the lack thereof in Cascadia. This could be explained by the availability of melt or the thicker (30 - 80 km) overriding plates acting as permeability barriers to deeper melt.

The presence of partial melt, its migration and ponding at the base of the lithosphere and small-scale convection in the asthenosphere has several implications for our understanding of lithosphere-asthenosphere interactions. Small-scale convection models typically require tens of millions of years for lithospheric gravitational instabilities to form and the lithospheric “drip” at 30 My seafloor age is consistent with onset times for small-scale convection for realistic mantle rheologies (e.g, Buck & Parmentier, 1986; Davaille & Jaupart, 1994) (Ballmer et al., 2009; Doin & Fleitout, 1996; King & Anderson, 1998; Korenaga & Jordan, 2003; Ritzwoller et al., 2004; van Hunen et al., 2003). However, for small-scale convection to occur at < 10 My seafloor age very low mantle viscosities ($\sim 10^{17}$ Pa s) are required (Buck & Parmentier, 1986). The presence of partial melt can effectively reduce the mantle viscosity by an order of magnitude or more (Jackson et al., 2006) and could allow small-scale convection to initiate at young ages. In addition, if partial melt in the asthenosphere coalesces, it could form positively buoyant instabilities that could seed small-scale convection from below (Barnouin-Jha & Parmentier, 1997) as the melt migrates through the asthenosphere and eventually ponds at the base of the lithosphere. Such melt and upwelling may cause a different pattern of small-scale convection than that predicted by previous modelling work. The large age offsets in the region caused by the Romanche and Chain Fracture zones, could also result in edge driven convection (King & Anderson, 1998) or shear driven upwelling (Ballmer et al., 2013) and stimulate small-scale convection at young ages. Upwelling at the ridge could potentially enhance this effect and begin

convection at relatively young seafloor ages. Future work will need to examine the role of melt for enhancing convection and melt migration and its effects on lithospheric evolution.

5. Conclusions

We image the lithosphere and asthenosphere beneath 0-80 My age seafloor at the equatorial Mid Atlantic. We observe a seismic fast lid that increases in thickness from 30 km at the ridge to 50 - 80 km on >60 My seafloor. The lid thickness increases away from the ridge to first order, and this occurs monotonically in some locations; whereas, in other locations the lid undulates in thickness and it is both thinner and thicker than predicted by conductive cooling models. In the asthenosphere, we observe punctuated low velocity regions with shear velocities < 4.1 km/s, which likely require melt. They are not necessarily focused beneath the ridge axis and extend to 400 km off-axis. These anomalies combined with what appears to be a lithospheric drip, suggest small-scale convection may be active at relatively young ages. A thick lithosphere in our region may be an effective permeability boundary, which could explain a lack of off-axis volcanism. The upwellings may feed melt channels that have been observed in active source studies. The implication is that melt and small-scale convection may interact dynamically with important implications for our understanding of heat flow and the thermal evolution of the ocean lithosphere.

Acknowledgements

Data used in this study are archived at the IRIS (Incorporated Research Institutions for Seismology) data management center (<http://ds.iris.edu/ds/nodes/dmc>) under the XS network for 2016-2017 (https://doi.org/10.7914/SN/XS_2016). The authors acknowledge funding from the Natural Environment Research Council (NE/M003507/1 and NE/K010654/1) and the European Research Council (GA 638665).

Figure 1 is a bathymetric map of the Mid-Atlantic Ridge (MAR) and surrounding regions. The map displays depth contours from 10 to 70 meters. Key features include the Romanche Fracture Zone (RFZ) and the Chain Fracture Zone (CFZ). Sampling stations are marked with circles (L and S series) and crosses (X). A color scale at the bottom indicates bathymetry from -8000 to -2000 meters. An inset map shows the location of the study area in the Atlantic Ocean.

Figure 1. Location map of the PI-LAB experiment. The Mid Atlantic Ridge is outlined in gray, circles show deployment locations, circles with x's show stations that did not return usable data.

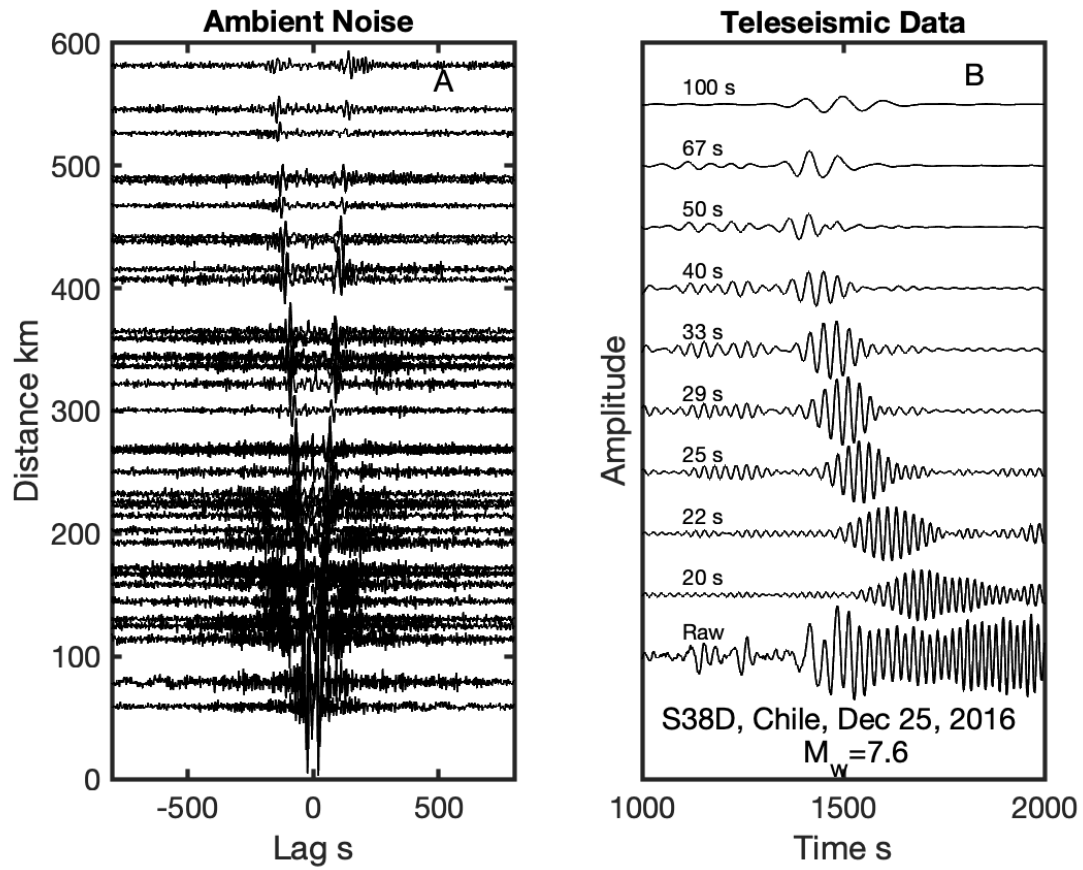


Figure 2. Data example for (A) ambient noise vertical noise correlation functions (NCF) and (B) teleseismic data from station S38D from the Christmas day M_w 7.6 Chile earthquake.

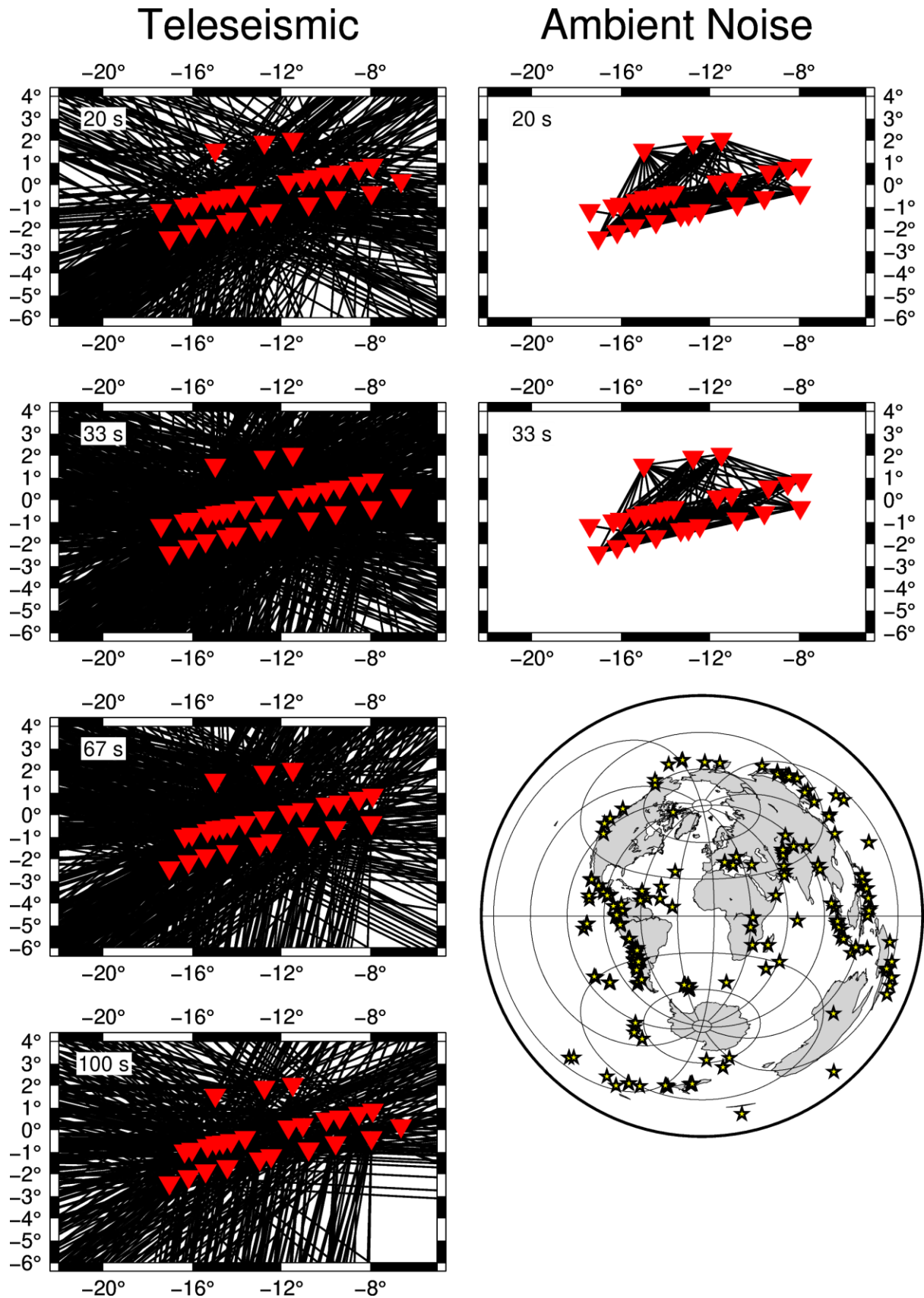


Figure 3. Example raypaths at select periods for the teleseismic data and ambient noise. Global map shows locations of earthquake sources as yellow stars used in the teleseismic study.

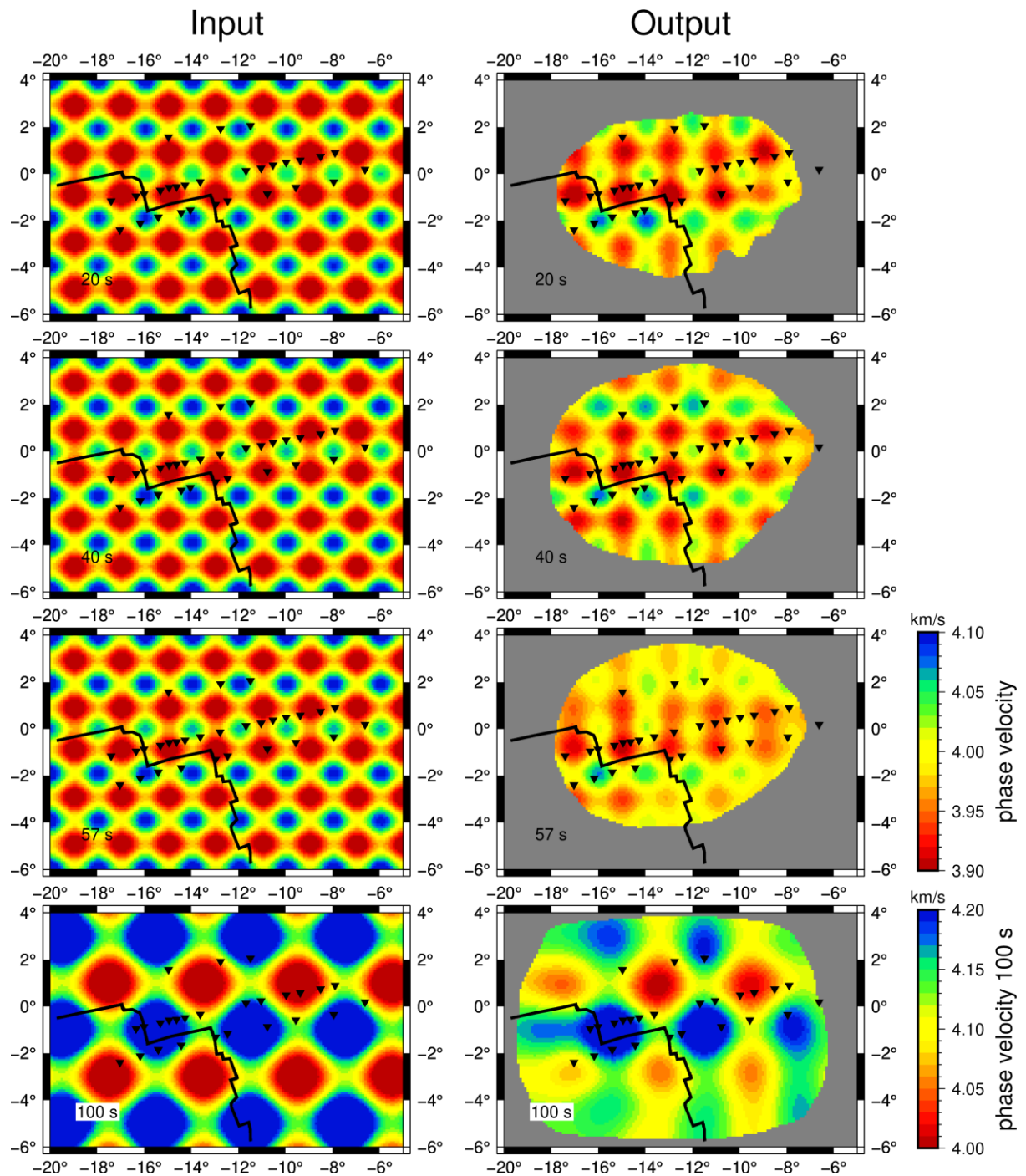


Figure 4. Checkerboard tests for 20, 40, 57 and 100 s period, with 1 degree and 2 degree anomaly sizes. Input model is shown on the left and output is shown on the right, with the period indicated within the figure.

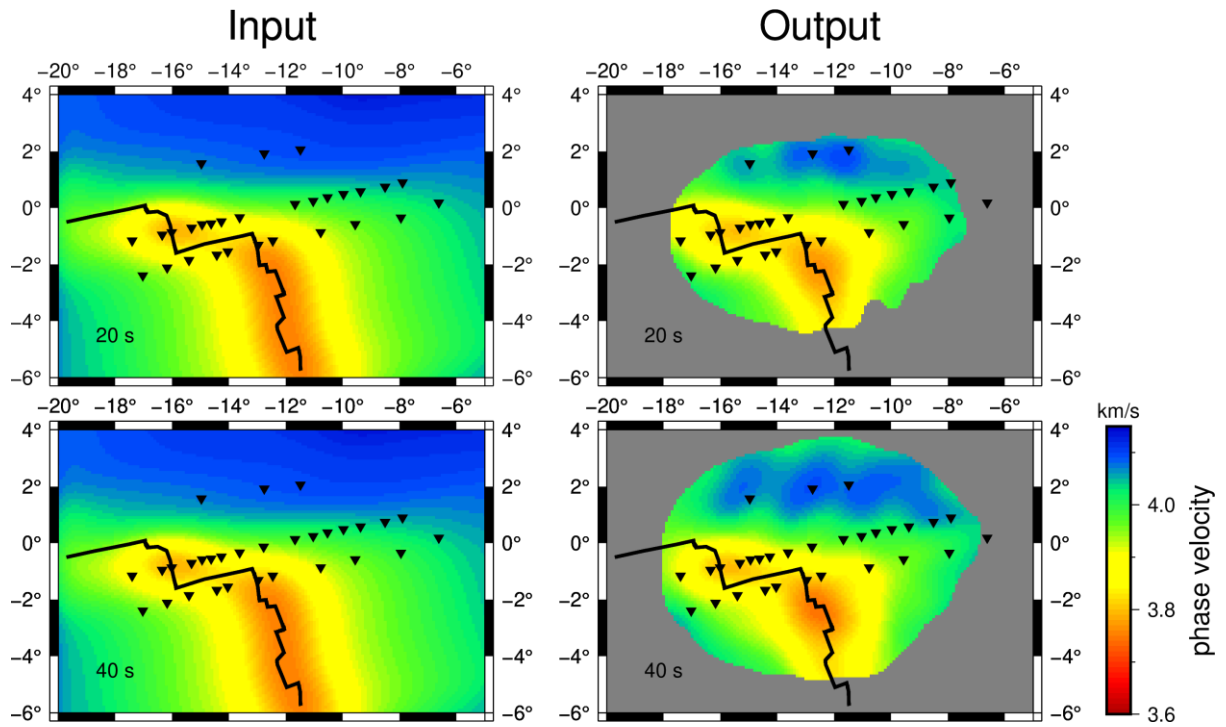


Figure 5. Structural recovery tests for 20 and 40 s period. Input model is shown on the left and output model is shown on the right. Period is indicated in the figure panel.

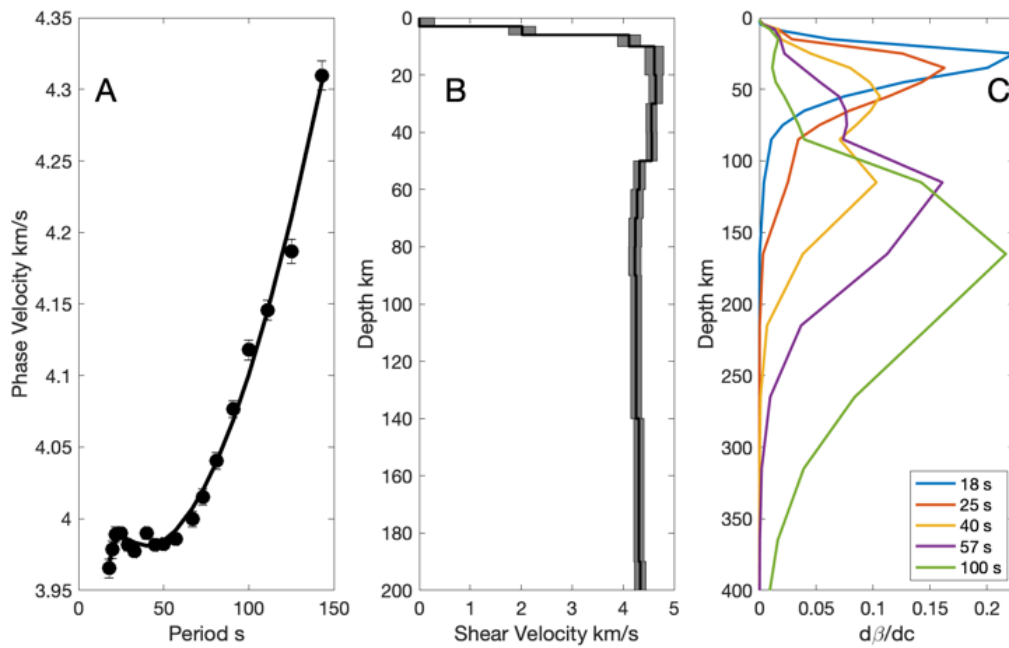


Figure 6. (A) Average dispersion curve for the region, with predicted dispersion curve (black line) , (B) preferred shear velocity model for the region with 2x standard error bar shown as grey shaded region. (C) Depth sensitivity kernels for different periods used in this study.

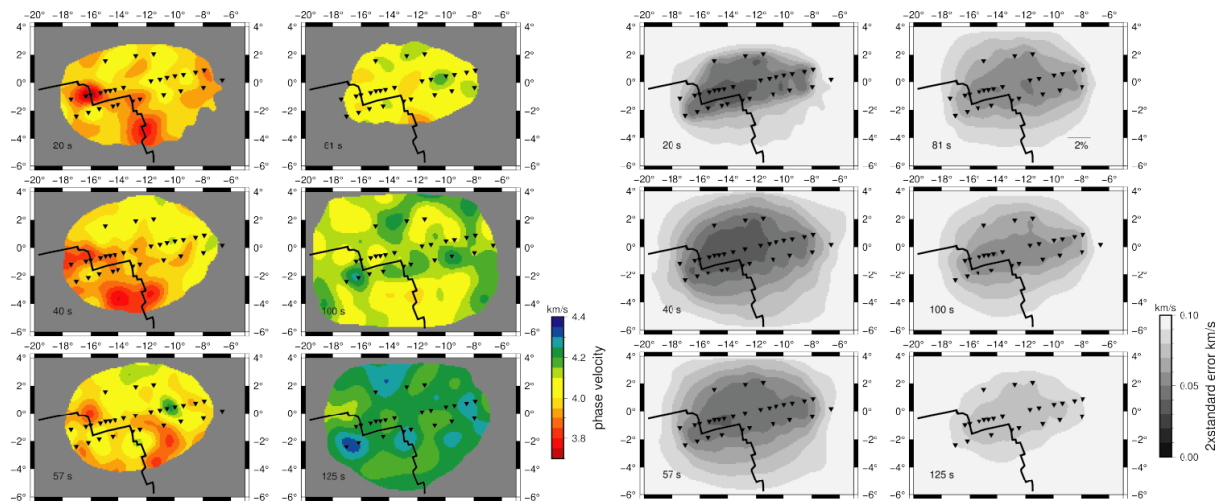


Figure 7. Phase velocity (color) and 2xstandard error maps (gray scale) at selected periods from 20-125 s. Stations are plotted as black triangles, and the Mid Atlantic Ridge is shown as a black line.

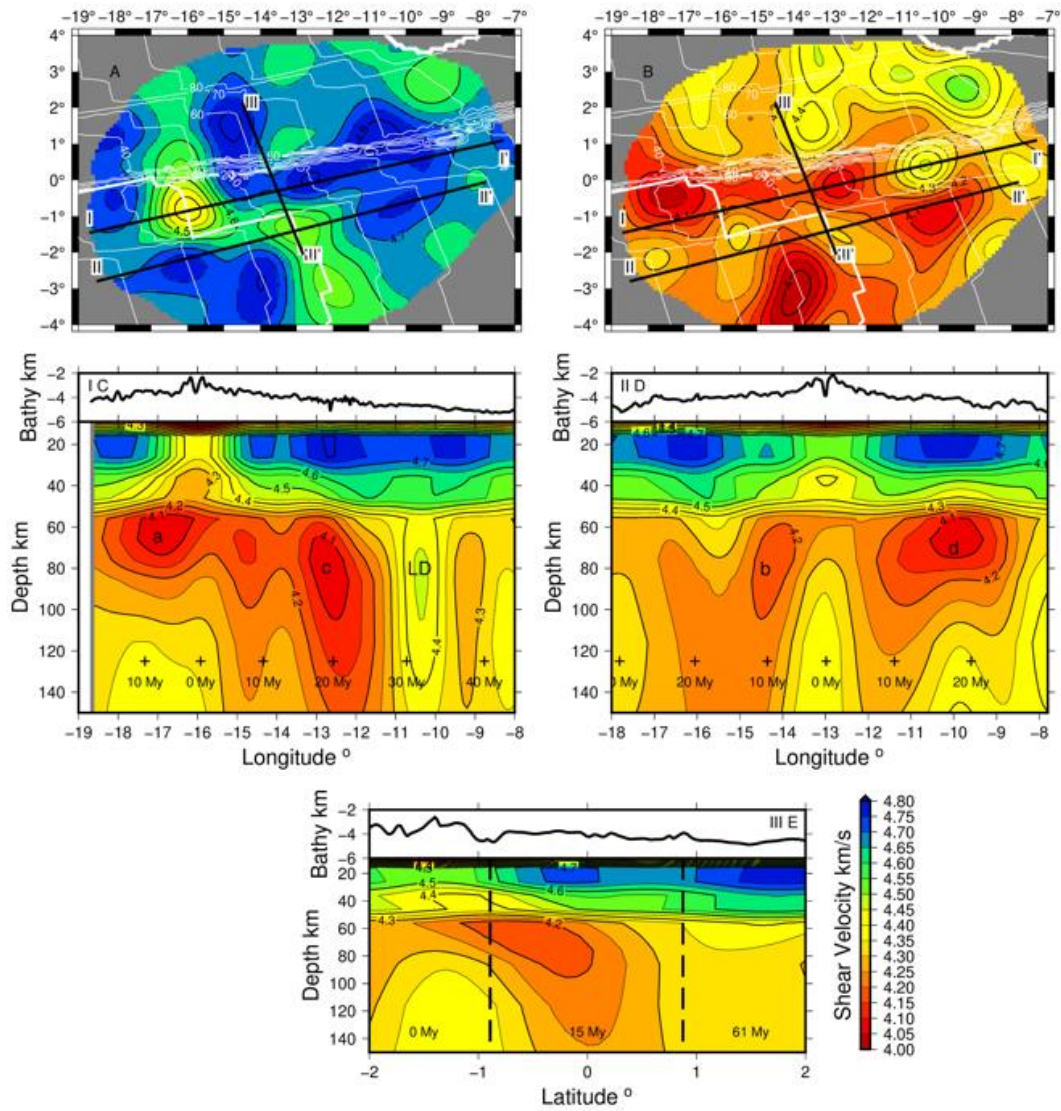


Figure 8. Shear Velocity model from discontinuous parameterization. (A) Shear velocity depth slice contoured at 0.05 km/s at 26 km depth, (B) depth slice contoured at 0.05 km/s at 76 km depth. Ridge is shown as a thick white line with 10 My seafloor age contours as thin white lines. Profiles I, II, and III in panels C-E. Profile plots are shown as indicated on the map. Anomalies of interest are labelled a-d and LD. Dashed lines in (E) show the locations of the fracture zones.

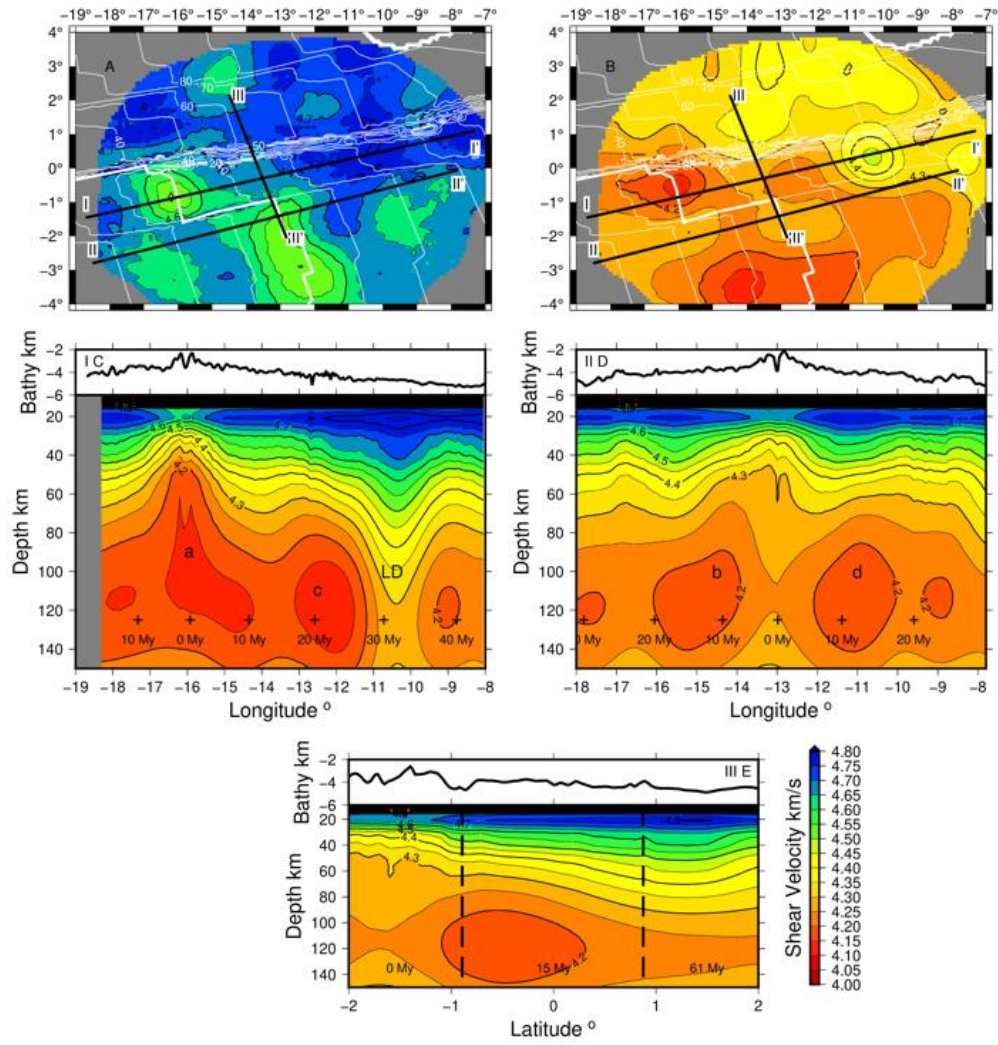


Figure 9. Shear velocity model with spline parameterization. Same presentation as Figure 8.

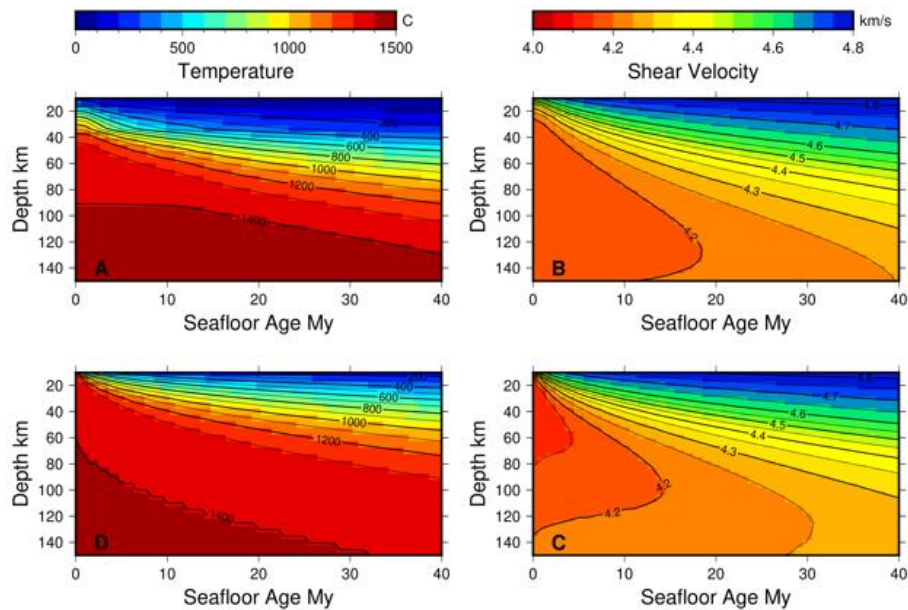


Figure 10. Spreading ridge geodynamic models and predicted shear velocities: (A) numerical geodynamic model with lateral conductive cooling and (B) corresponding shear velocity prediction, (C) half-space cooling model and (D) its corresponding shear velocity prediction. Temperatures and shear velocities are contoured as indicated.

References

- Agius, M., Harmon, N., Rychert, C. A., Tharimena, S., & Kendall, J. M. (2018). Sediment Characterization at the Equatorial Mid-Atlantic Ridge From P-to-S Teleseismic Phase Conversions Recorded on the PI-LAB Experiment. *Geophysical Research Letters*, 45. doi:<https://doi.org/10.1029/2018GL080565>
- Ballmer, M. D., Conrad, C. P., Smith, E. I., & Harmon, N. (2013). Non-hotspot volcano chains produced by migration of shear-driven upwelling toward the East Pacific Rise. *Geology*, 41(4), 479-482. doi:10.1130/G33804.1
- Ballmer, M. D., Ito, G., van Hunen, J., Bianco, T. A., & Tackley, P. J. (2009). Small-scale sublithospheric convection reconciles geochemistry and geochronology of intraplate volcanoes in the W- and S-Pacific. *Geochimica Et Cosmochimica Acta*, 73(13), A81-A81.
- Barnouin-Jha, K., & Parmentier, E. M. (1997). Buoyant mantle upwelling and crustal production at oceanic spreading centers: On-axis and off-axis melting. *J. Geophys. Res.*, 102(B6), 11979-11989.
- Behn, M. D., Hirth, G., & Elsenbeck, J. R. (2009). Implications of grain size evolution on the seismic structure of the oceanic upper mantle. *Earth and Planetary Science Letters*, 282(1-4), 178-189. doi:10.1016/j.epsl.2009.03.014
- Bell, S., Ruan, Y. Y., & Forsyth, D. W. (2016). Ridge asymmetry and deep aqueous alteration at the trench observed from Rayleigh wave tomography of the Juan de Fuca plate. *Journal of Geophysical Research-Solid Earth*, 121(10), 7298-7321. doi:10.1002/2016jb012990

- Bensen, G. D., Ritzwoller, M. H., Barmin, M. P., Levshin, A. L., Lin, F., Moschetti, M. P., . . . Yang, Y. (2007). Processing seismic ambient noise data to obtain reliable broad-band surface wave dispersion measurements. *Geophys. J. Int.*, *169*, doi: 10.1111/j.1365-1246X.2007.03374.x.
- Buck, W. R., & Parmentier, E. M. (1986). Convection beneath young oceanic lithosphere; implications for thermal structure and gravity. *J. Geophys. Res.*, *91*(2), 1961-1974.
- Buck, W. R., & Su, W. S. (1989). Focused Mantle Upwelling Below Mid-Ocean Ridges Due to Feedback between Viscosity and Melting. *Geophysical Research Letters*, *16*(7), 641-644. doi:DOI 10.1029/GL016i007p00641
- Davaille, A., & Jaupart, C. (1994). Onset of convection in fluids with temperature-dependent viscosity: Application to the oceanic mantle. *J. Geophys. Res.*, *99*(B10), 19,853-819,866.
- Doin, M. P., & Fleitout, L. (1996). Thermal evolution of the oceanic lithosphere: An alternative view. *Earth and Planetary Science Letters*, *142*(1-2), 121-136. doi:Doi 10.1016/0012-821x(96)00082-9
- Forsyth, D., & Uyeda, S. (1975). Relative Importance of Driving Forces of Plate Motion. *Geophysical Journal of the Royal Astronomical Society*, *43*(1), 163-200. doi:DOI 10.1111/j.1365-246X.1975.tb00631.x
- Forsyth, D. W. (1992). Geophysical Constraints on Mantle Flow and Melt Generation Beneath Mid-Ocean Ridges. In J. Phipps Morgan, D. K. Blackman, & J. M. Sinton (Eds.), *Mantle Flow and Melt Generation at Mid-Ocean Ridges, Geophysical Monograph* (Vol. 71, pp. 1-65). Washington, DC: AGU.
- Forsyth, D. W., & Li, A. (2005). Array-analysis of two-dimensional variations in surface wave phase velocity and azimuthal anisotropy in the presence of multipathing interference. In A. Levander & G. Nolet (Eds.), *Seismic Data Analysis and Imaging with Global and Local Arrays: AGU Monograph*.
- Forsyth, D. W., Scheirer, D. S., Webb, S. C., Dorman, L. M., Orcutt, J. A., Harding, A. J., . . . Melt Seismic Team, U. S. (1998). Imaging the deep seismic structure beneath a mid-ocean ridge; the MELT experiment. *Science*, *280*(5367), 1215-1218.
- Gaherty, J. B., Jordan, T. H., & Gee, L. S. (1996). Seismic structure of the upper mantle in a central Pacific corridor. *J. Geophys. Res.*, *101*(B10), 22,291-222,309.
- Hammond, W. C., & Humphreys, E. D. (2000). Upper mantle seismic wave velocity: Effects of realistic partial melt geometries. *J. Geophys. Res.*, *105*(5), 10975-10986.
- Harmon, N., Forsyth, D. W., & Weeraratne, D. S. (2009). Thickening of Young Pacific Lithosphere From High-Resolution Rayleigh Wave Tomography: A Test of the Conductive Cooling Model. *Earth Plan. Sci. Lett.*, *278*(1-2), 96-106.
- Harmon, N., Gerstoft, P., Rychert, C. A., Abers, G. A., Salas de la Cruz, M., & Fischer, K. M. (2008). Phase velocities from seismic noise using beamforming and cross correlation in Costa Rica and Nicaragua. *Geophysical Research Letters*, *35*(L19303), doi:10.1029/2008GL03587.
- Harmon, N., & Rychert, C. A. (2016). Joint inversion of teleseismic and ambient noise Rayleigh waves for phase velocity maps, an application to Iceland. *Journal of Geophysical Research-Solid Earth*, *121*(8), 5966-5987. doi:10.1002/2016jb012934
- Harmon, N., Rychert, C. A., Agius, M. R., Tharimena, S., Le Bas, T. P., Kendall, J. M., & Constable, S. (2018). Marine geophysical investigation of the Chain Fracture Zone in the equatorial Atlantic from the PI-LAB Experiment. *J. Geophys. Res.*, *123*, 11,016–011,030. doi:10.1029/2018JB015982

- Harmon, N., Rychert, C. A., & Gerstoft, P. (2010). Distribution of Noise Sources for Seismic Interometry. *Geophys. J. Int.*, 183(3), doi: 10.1111/j.1365-1246X.2010.04802.x.
- Hasterok, D., Chapman, D. S., & Davis, E. E. (2011). Oceanic heat flow: Implications for global heat loss. *Earth and Planetary Science Letters*, 311(3-4), 386-395. doi:10.1016/j.epsl.2011.09.044
- Havlin, C., Parmentier, E. M., & Hirth, G. (2013). Dike propagation driven by melt accumulation at the lithosphere-asthenosphere boundary. *Earth and Planetary Science Letters*, 376, 20-28. doi:10.1016/j.epsl.2013.06.010
- Hawley, W. B., Allen, R. M., & Richards, M. A. (2016). Tomography reveals buoyant asthenosphere accumulating beneath the Juan de Fuca plate. *Science*, 353(6306), 1406-1408. doi:10.1126/science.aad8104
- Jackson, I., & Faul, U. H. (2010). Grainsize-sensitive viscoelastic relaxation in olivine: Towards a robust laboratory-based model for seismological application. *Phys. Earth Plan. Inter.*, 183(1-2), 151-163. doi:Doi 10.1016/J.Pepi.2010.09.005
- Jackson, I., Faul, U. H., Fitz Gerald, J. D., & Morris, S. J. S. (2006). Contrasting viscoelastic behavior of melt-free and melt-bearing olivine: Implications for the nature of grain-boundary sliding. *Materials Science and Engineering a-Structural Materials Properties Microstructure and Processing*, 442(1-2), 170-174. doi:Doi 10.1016/J.Msea.2006.01.136
- Jha, K., Parmentier, E. M., & Morgan, J. P. (1994). The Role of Mantle-Depletion and Melt-Retention Buoyancy in Spreading-Center Segmentation. *Earth and Planetary Science Letters*, 125(1-4), 221-234.
- Karlsen, K. S., Conrad, C. P., & Magni, V. (2019). Deep Water Cycling and Sea Level Change Since the Breakup of Pangea. *Geochemistry Geophysics Geosystems*, 20(6), 2919-2935. doi:10.1029/2019gc008232
- King, S. D., & Anderson, D. L. (1998). Edge-driven convection. *Earth Plan. Sci. Lett.*, 160(3-4), 289-296.
- Korenaga, J., & Jordan, T. H. (2003). Linear Stability of Richter Rolls. *Geophys. Res. Lett.*, 30(22), doi:10.1029/2003GL018337.
- Korenaga, T., & Korenaga, J. (2008). Subsidence of normal oceanic lithosphere, apparent thermal expansivity, and seafloor flattening. *Earth Planet. Sci. Lett.*, 268(1-2), 41-51. doi:Doi 10.1016/J.Epsl.2007.12.022
- Landisman, M., Dziewonski, A., & Sato, Y. (1969). Recent improvements in the analysis of surface wave observations. *Geophys. J. Roy. Ast. Soc.*, 17(4), 369-403.
- Levshin, A. L., & Ritzwoller, M. H. (2001). Automated detection, extraction, and measurement of regional surface waves. *Pure and Applied Geophysics*, 158(8), 1531-1545. doi:Doi 10.1007/Pl00001233
- Mehouachi, F., & Singh, S. (2018). Water-rich sublithospheric melt channel in the equatorial Atlantic Ocean. *Nat. Geosci.*, 11, 65-69. doi:doi:10.1038/s41561-017-0034-z
- Morgan, J. P., Parmentier, E. M., & Lin, J. (1987). Mechanisms for the origin of midocean ridge axial topography - Implications for the thermal and mechanical structure of accreting plate boundaries. *Journal of Geophysical Research*, 92(B12), 12823-12836. doi:DOI 10.1029/JB092iB12p12823
- Parmentier, E. M., & Morgan, J. P. (1990). Spreading Rate Dependence of 3-Dimensional Structure in Oceanic Spreading Centers. *Nature*, 348(6299), 325-328. doi:Doi 10.1038/348325a0

- Parsons, B., & Sclater, J. G. (1977). Analysis of Variation of Ocean-Floor Bathymetry and Heat-Flow with Age. *J. Geophys. Res.*, 82(5), 803-827.
- Richter, F. M. (1973). Convection and large-scale circulation of mantle. *Journal of Geophysical Research*, 78(35), 8735-8745.
- Ritzwoller, M. H., Shapiro, N. M., & Zhong, S. J. (2004). Cooling history of the Pacific lithosphere. *Earth Plan. Sci. Lett.*, 226(1-2), 69-84.
- Rychert, C., Harmon, N., Constable, S., Kendall, J., Tharimena, S., Wang, S., . . . Hicks, S. (2019). A dynamic lithosphere-asthenosphere boundary dictated by variations in melt generation and migration: Results from the PI-LAB Experiment in the Equatorial Mid Atlantic. Paper presented at the American Geophysical Union, San Francisco, CA, USA.
- Rychert, C. A., Harmon, N., & Tharimena, S. (2018). Scattered wave imaging of the oceanic plate in Cascadia. *Science Advances*, 4(2). doi:ARTN eaao1908 10.1126/sciadv.aao1908
- Saito, M. (1988). DISPER80: A subroutine package for the calculation of seismic normal-mode solutions. In D. J. Doornbos (Ed.), *Seismological Algorithms: Computational Methods and Computer Programs* (pp. 293-319). San Diego: Academic Press.
- Schilling, J. G., Hanan, B. B., Mccully, B., Kingsley, R. H., & Fontignie, D. (1994). Influence of the Sierra-Leone Mantle Plume on the Equatorial Mid-Atlantic Ridge - a Nd-Sr-Pb Isotopic Study. *Journal of Geophysical Research-Solid Earth*, 99(B6), 12005-12028. doi:Doi 10.1029/94jb00337
- Schilling, J. G., Ruppel, C., Davis, A. N., Mccully, B., Tighe, S. A., Kingsley, R. H., & Lin, J. (1995). Thermal Structure of the Mantle beneath the Equatorial Mid-Atlantic Ridge - Inferences from the Spatial Variation of Dredged Basalt Glass Compositions. *Journal of Geophysical Research-Solid Earth*, 100(B6), 10057-10076. doi:Doi 10.1029/95jb00668
- Stein, S., & Stein, C. A. (1992). A model for the global variation in oceanic depth and heat flow with lithospheric age. *Nature*, 359(6391), 123-129.
- Stern, R. L. (2002). Subduction Zones. *Rev. of Geophys.*, 40(4), 3-1-3-38. doi:<https://doi.org/10.1029/2001RG000108>
- Stern, T. A., Henrys, S. A., Okaya, D., Louie, J. N., Savage, M. K., Lamb, S., . . . Iwasaki, T. (2015). A seismic reflection image for the base of a tectonic plate. *Nature*, 518(7537), 85-+. doi:10.1038/nature14146
- Stixrude, L., & Lithgow-Bertelloni, C. (2005). Mineralogy and elasticity of the oceanic upper mantle: Origin of the low-velocity zone. *J. Geophys. Res.*, 110, B03204, 03210.1029/02004JB002965.
- Tarantola, A., & Valette, B. (1982). Generalized nonlinear inverse problems solved using the least squares criterion. *Rev. of Geophys. and Space Phys.*, 20(2), 219-232.
- Toomey, D. R., Allen, R. M., Barclay, A. H., Bell, S. W., Bromirski, P. D., Carlson, R. L., . . . Wilcock, W. S. D. (2014). THE CASCADIA INITIATIVE A Sea Change In Seismological Studies of Subduction Zones. *Oceanography*, 27(2), 138-150.
- Turcotte, D., & Oxburgh, E. R. (1967). Finite amplitude convective cells and continental drift. *J. Fluid Mech.*, 28(1), 29-42.
- van Hunen, J., Huang, J., & Zhong, S. (2003). The effect of shearing on the onset and vigor of small-scale convection in a Newtonian rheology. *Geophys. Res. Lett.*, 30(19), doi:10.1029/2003GL018101.

- Wang, S., Constable, C. G., Rychert, C. A., & Harmon, N. (2020). A lithosphere-asthenosphere boundary and partial melt estimated using marine magnetotelluric data at the central Middle Atlantic Ridge. *Submitted to Geochem. Geophys. Geosys.*
- Weeraratne, D. S., Forsyth, D. W., Yang, Y., & Webb, S. C. (2007). Rayleigh wave tomography beneath intraplate volcanic ridges in the South Pacific. *J. Geophys. Res.*, *112*, B06303, doi:06310.01029/02006JB00440.
- Yang, Y., & Forsyth, D. W. (2006). Rayleigh wave phase velocities, small-scale convection, and azimuthal anisotropy beneath southern California. *J. Geophys. Res.*, *111*, B07306, doi:07310.01029/02005JB004180.
- Zhou, Y., Dahlen, F. A., & Nolet, G. (2004). Three-dimensional sensitivity kernels for surface wave observables. *Geophys. J. Int.*, *158*(1), 142-168.